ACS NANO
Cite This: ACS Nano 2017, 11, 10222-10229
www.acsnano.org

ARTICLE

Controlled Growth of a Large-Size 2D Selenium Nanosheet and Its Electronic and Optoelectronic Applications

Jingkai Qin,[†,§,#] Gang Qiu,[†,#] Jie Jian,[‡] Hong Zhou,[†] Lingming Yang,[†] Adam Charnas,[†] Dmitry Y. Zemlyanov,[†] Cheng-Yan Xu,[§] Xianfan Xu,[∥] Wenzhuo Wu,[⊥] Haiyan Wang,[†,‡] and Peide D. Ye*[,†]

[†]School of Electrical and Computer Engineering, Purdue University, West Lafayette, Indiana 47907, United States
[‡]School of Materials Science and Engineering, Purdue University, West Lafayette, Indiana 47907, United States
[§]School of Materials Science and Engineering, Harbin Institute of Technology, Harbin 150001, People's Republic of China
[∥]School of Mechanical Engineering, Purdue University, West Lafayette, Indiana 47907, United States
[⊥]School of Industry Engineering, Purdue University, West Lafayette, Indiana 47907, United States

S *Supporting Information*

ABSTRACT: **Selenium has attracted intensive attention as a promising material candidate for future optoelectronic applications. However, selenium has a strong tendency to grow into nanowire forms due to its anisotropic atomic structure, which has largely hindered the exploration of its potential applications. In this work, using a physical vapor deposition method, we have demonstrated the synthesis of large-size, high-quality 2D selenium nanosheets, the minimum thickness of which could be as thin as 5 nm. The Se nanosheet exhibits a strong in-plane anisotropic property, which is determined by angle-resolved Raman spectroscopy. Back-gating field-effect transistors based on a Se nanosheet exhibit p-type transport behaviors with on-state current density around 20 mA/mm at V_{ds} = 3 V. Four-terminal field-effect devices are also fabricated to evaluate the intrinsic hole mobility of the selenium nanosheet, and the value is determined to be 0.26 $cm^2 V^{-1} s^{-1}$ at 300 K. The selenium nanosheet phototransistors show an excellent photoresponsivity of up to 263 A/W, with a rise time of 0.1 s and fall time of 0.12 s. These results suggest that crystal selenium as a 2D form of a 1D van der Waals solid opens up the possibility to explore device applications.**

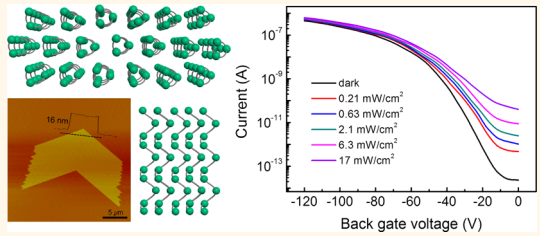

KEYWORDS: *selenium, 1D crystal structure, 2D nanosheet, electrical transport, photoresponse*

Trigonal selenium (*t*-Se) is a one-dimensional elemental semiconductor material, in which Se atoms are covalently connected in a spiral chain along the *c*-axis with two adjacent atoms rotated by 120°. As shown in Figure 1a and b, all these atomic chains are stacked together in their radical direction by weak van der Waals interactions to form a hexagonal lattice structure. *t*-Se has attracted extensive attention due to its interesting properties such as high photoconductivity,[1−5] high piezoelectricity,[6−8] thermoelectricity,[9] and nonlinear optical responses.[10,11] The high photoconductivity makes it a promising candidate for applications in high-efficiency solar cells and optoelectronic devices.[12,13] Recent reports have shown that Se nanosheet photodetectors exhibit a high responsivity of 100 mA/W at 620 nm light illumination with an ultrashort rise/decay time (1.4/7.8 ms).[14]

A variety of Se-based nanostructures have been obtained by different synthesis methods, such as a hydrothermal solution process and microwave-assisted synthesis in ionic liquids.[14,15] Compared with solution-based techniques, which always introduce impurities due to the complex chemical processes involved, a vapor phase approach should be more efficient to obtain high-quality products.[16,17] Due to the anisotropic chain-like crystal structure, Se tends to form 1D structures, such as nanowires, nanotubes, and nanobelts. These 1D structures with a high ratio of edges to bulk always exhibit poor electrical transport behaviors due to localized states and contacts, and the issue of electrical noise becomes critical with decreasing size, as described by Hooge's rule.[18,19] To expand its applications in high-performance electronic and optoelectronic devices, it would be useful to expand Se nanostructures to a two-dimensional form.

Received: July 7, 2017
Accepted: September 26, 2017
Published: September 26, 2017

DOI: 10.1021/acsnano.7b04786
ACS Nano 2017, 11, 10222−10229

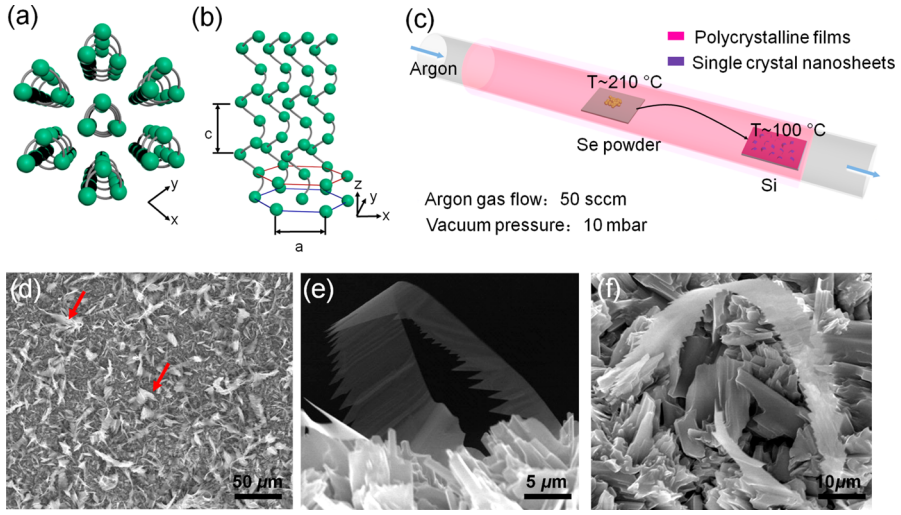

Figure 1. PVD-grown large-area Se nanosheets and material characterization. (a, b) Atomic structure of selenium. (c) Schematic diagram of the PVD method. (d) Low-magnification SEM image of as-prepared selenium nanosheets on a Si(111) substrate. (e) Enlarged view of typical Se nanosheets with saw-like structure and (f) feather-like twin structure.

Recently, tellurium (Te), which possesses the same crystal structure as Se, has been successfully synthesized in a 2D form using a substrate-free solution process, and 2D tellurium (termed as tellurene) flakes exhibit strong in-plane anisotropic properties and high carrier mobility.[20−22] Inspired by this success, using a physical vapor deposition (PVD) method, we successfully obtained highly crystalline Se nanosheets with interesting zigzag edge structure, with a minimum thickness of Se of 5 nm. Scanning transmission electron microscopy (STEM) and angle-resolved Raman spectroscopy confirm that the single-crystal Se nanosheet has an oriented growth direction along $\langle 1\bar{2}10 \rangle$, which is very different from previous studies.[16,17] To the best of our knowledge, no works have been reported on the synthesis of such large-size 2D ultrathin Se nanosheets. Back-gated field-effect transistors (FETs) based on our 2D PVD-grown Se nanosheet exhibit p-type transport behaviors with on-state current density around 20 mA/mm at V_{ds} = 3 V. Four-terminal field-effect devices are also fabricated to evaluate the intrinsic hole mobility of the Se nanosheet, and the value is determined to be 0.26 $cm^2\ V^{-1}\ s^{-1}$ at 300 K. Se nanosheet phototransistors are found to have an excellent photoresponsivity (263 A/W) with a 0.10 s rise time and a 0.12 s fall time. This work demonstrates that the crystal selenium nanosheet, which is built up by 1D van der Waals material selenium, has very interesting properties for further exploration of device applications as a type of 2D semiconductor material.

RESULTS AND DISCUSSION

The Se nanosheets were obtained using the PVD method, and the typical growth setup used is illustrated in Figure 1c. Se powder was placed in a quartz glass tube as the precursor. A plan-view SEM image of Se nanosheets as-grown on a Si substrate is shown in Figure 1d, in which inclined nanosheets (as indicated by arrows) with a density of more than 50% were uniformly distributed on the surface of polycrystalline Se films. Figure 1e shows the representative morphology of the Se nanosheets at high magnification in SEM. Most of the nanosheets exhibit a saw-like structure with zigzag edges on the single narrow side. The average width of the nanosheets is about 8 μm, and the maximum length of the nanosheets could reach up to 50 μm. In the SEM images, the nanosheets are almost electron transparent, suggesting that they are very thin. It is worth noting that about 10% of the Se nanosheets have bilateral zigzag edges, exhibiting a feather-like structure (Figure 1f). The growth mechanism for these 2D Se nanosheets will be discussed in the following section.

To further indentify the surface morphology, we transferred the nanosheets onto a Si/SiO_2 substrate using the Scotch tape method (a typical transfer procedure is shown in Figure S1). Figure 2a shows the optical microscopy image of the Se nanosheets. Consistent with the SEM images, most of the Se nanosheets exhibit an irregular quadrangular shape with zigzag

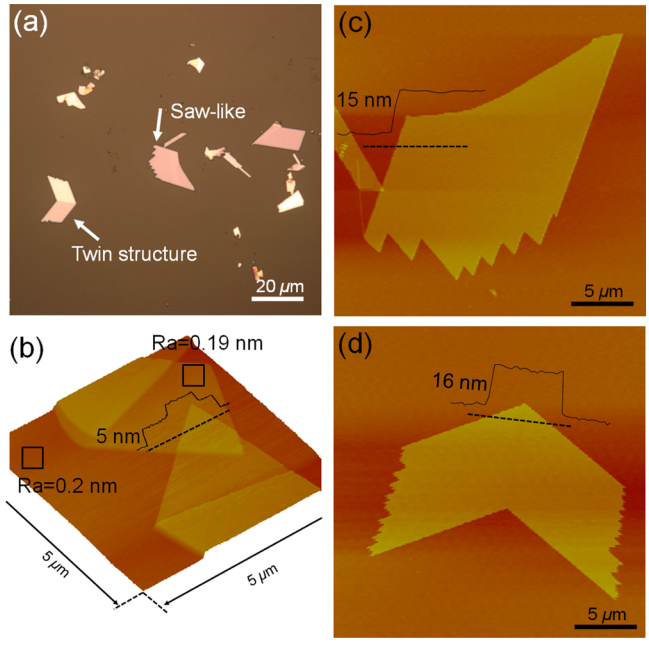

Figure 2. Optical and AFM characterization. (a) Optical microscopy image of samples after being transferred onto the SiO_2/Si substrate. (b) AFM topography image of a Se nanosheet with a thickness of 5 nm in 3D view, showing an atomically flat surface of the Se nanosheet. (c, d) AFM height profile of a saw-like and twin structure nanosheet.

DOI: 10.1021/acsnano.7b04786
ACS Nano 2017, 11, 10222−10229

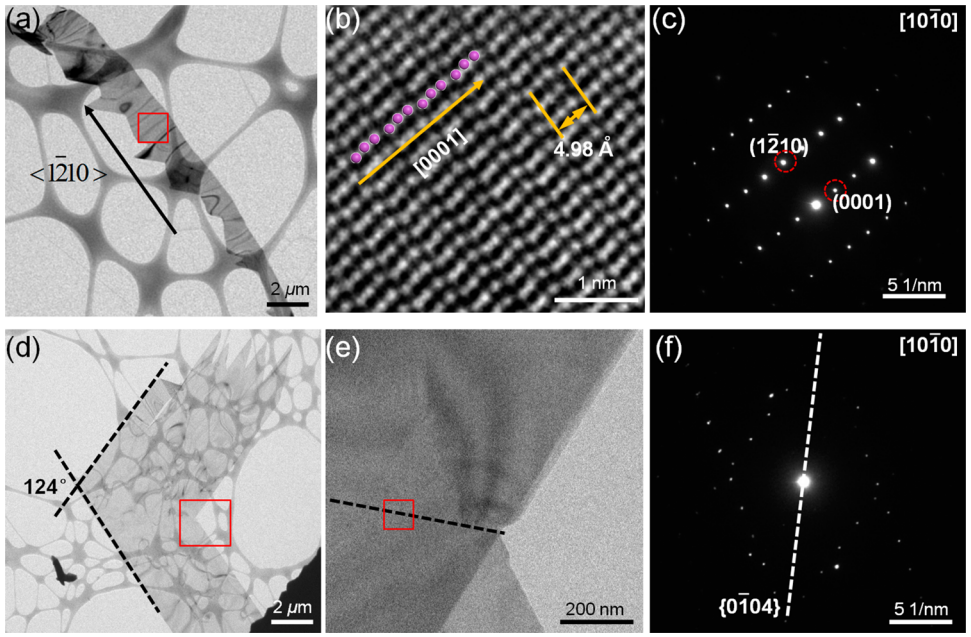

Figure 3. STEM characterization of a Se nanosheet. (a) Bright-field TEM image of Se nanosheets with saw-like structure. (b) HAADF-STEM image and (c) corresponding SAED pattern of Se nanosheets (boxed area in (a)). (d, e) Bright-field TEM image of feather-like Se nanosheets with different magnification. (f) SAED pattern obtained at the coherent crystal boundary (boxed area in (e)), with common spots showing the mutual twin boundary of the {0$\bar{1}$04} plane.

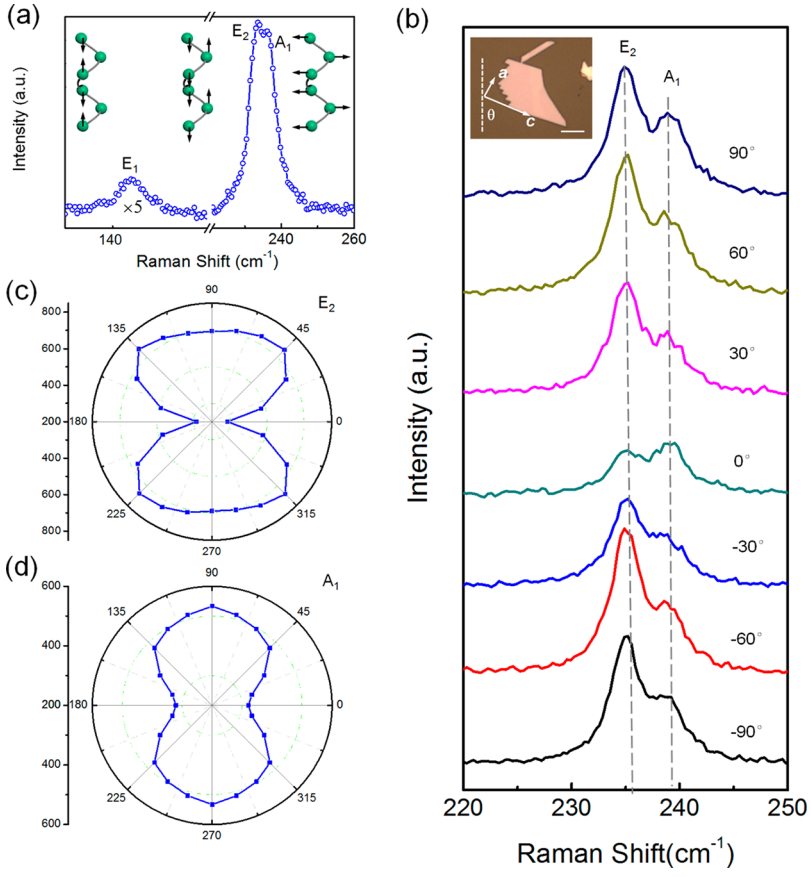

Figure 4. Angle-resolved Raman spectra for few-layer Se nanosheets. (a) Raman spectrum of a Se nanosheet with a thickness of 15 nm. The inset shows the atomic vibration patterns of E_1, E_2, and A_1 phonon modes in selenium. (b) Raman spectra evolution with angles between crystal orientation and incident laser polarization. (c, d) Polar figures of Raman intensity corresponding to E_2 and A_1 modes located at 233 and 237 cm^{-1}.

DOI: 10.1021/acsnano.7b04786
ACS Nano 2017, 11, 10222−10229

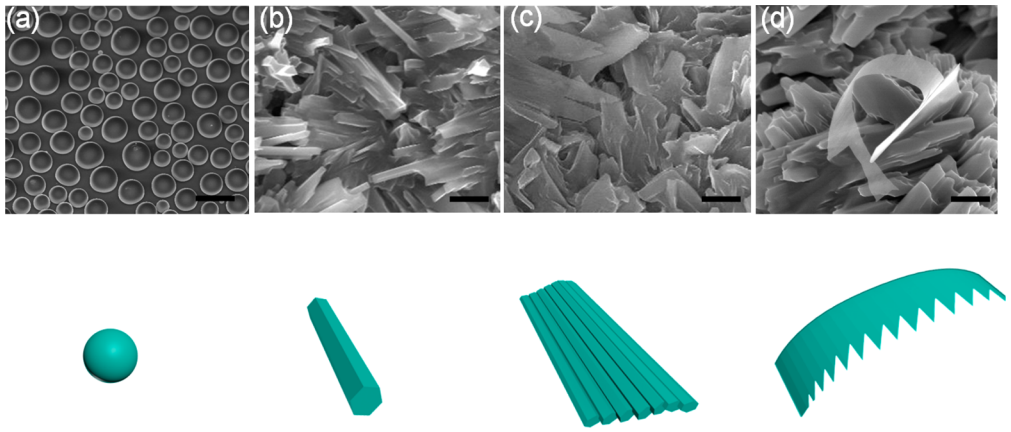

Figure 5. Growth mechanism of Se nanosheets: (a) 160 °C; scale bar is 20 μm; (b) 210 °C, 5 min; (c) 210 °C, 30 min; (d) 210 °C, 60 min; scale bar in (b, c) is 5 μm.

edges on a unilateral side, and the rest of them have twin structures with mirror symmetry. Atomic force microscopy (AFM) was employed to determine the thickness and topography of the nanosheets. As the 3D view shows in Figure 2b, the minimum measured thickness of the Se nanosheets is 5 nm, and the surface is atomically flat with a surface roughness (R_a) of 190 pm, even less than that of the SiO_2 surface (about 200 pm), indicating that the Se nanosheets are highly crystallized with good quality. Figure 2c and d show the height profiles of the saw-like and twin structure selenium nanosheets, with an average thickness of 15 nm. It should be noted that the twin structure could be clearly detected according to contrast difference by optical microscopy, while the corresponding AFM image shows a uniform height profile. This result suggests that the bicrystalline Se nanosheet divided from the middle has two separate single-crystal grains with different orientations. XPS analysis was also conducted to determine the quality of Se nanosheets (Figure S2).The strong peaks located at 55.5 and 54.3 eV correspond to Se $3d_{3/2}$ and $3d_{5/2}$ binding energy of $Se^{(0)}$, respectively. The Se 3d oxidized peak located 59.9 eV cannot be detected, indicating that the Se nanosheets are elemental crystals without obvious oxidation.[23,24]

Transmission electron microscopy (TEM) was employed to identify the microstructure and growth directions of the Se nanosheets. The nanosheets could be directly transferred onto Cu grids. The low-magnification bright-field TEM image (Figure 3a) shows a 2D saw-like structure, similar to what was observed in the optical microscopy image. The high-angle annular dark field STEM (HAADF-STEM) image could provide Z-contrast with atomic lateral resolution (Z = atomic number). As shown in Figure 3b, Se helical atomic chains could be clearly resolved with a fringe spacing of (0001) lattice planes of about 5.0 Å. The corresponding selected area electron diffraction (SAED) image, which was obtained along the $[10\bar{1}0]$ zone axis of an individual nanosheet, exhibits a set of 2-fold and rotational symmetry pattern, indicating the Se nanosheet is highly crystalline. Combined with the HAADF-STEM image and SAED pattern, we can determine that the Se nanosheets have first grown along the ⟨0001⟩ direction into nanoribbons, and then these nanoribbons expand in parallel along the $\langle 1\bar{2}10\rangle$ direction, leading to the formation of a large-area nanosheet with zigzag edges. TEM analysis was also conducted to determine the crystal structure of the feather-like Se nanosheets with twin structure. As the bright-field TEM images with different magnification show (Figure 3e and f), the angle of two twinned grains is about 124°. By carefully correlating the SAED pattern obtained from the boundary area (Figure 3g), it could be found that $\{0\bar{1}04\}$ diffraction spots are perpendicular to the twin boundary, indicating that the twin boundary is a $\{0\bar{1}04\}$ twin. EDX and EELS also confirmed that the synthesized nanosheet is an elemental Se crystal (Figure S3).

The in-plane anisotropy of the Se nanosheet is investigated by angle-resolved Raman spectroscopy at room temperature. The angle between the laser polarization direction and [0001] helical chain direction of the nanosheet is defined as θ, which could be tuned by rotating the sample in steps of 15° during measurement. Figure 4a shows the typical Raman spectrum of a 15 nm thick nanosheet with an angle θ of 45°. Consistent with the previous observations in bulk selenium,[25,26] three active Raman photon modes are clearly observed. Raman peaks located at ∼233 and 237 cm^{-1} are related to the E_2 and A_1 modes, respectively. Meanwhile, one degenerate E_1 mode caused by a-axis rotation is also indentified. Figure 4b depicts the evolution of the Raman spectrum as the sample is rotated in steps of 30° from −90° to 90°, and a clear intensity change could be observed. The peak intensities of different modes are extracted by fitting with a Gauss function and plotted into the corresponding polar figures (Figure 4c,d). It should be noted that the degenerate E_1 mode is hard to extract due to the relatively weak intensity. Both the E_2 and A_1 modes exhibit significant intensity change with the polarization angle. The A_1 mode is a maximum at an angle of ∼90°, which corresponds to the direction vertical to the Se chains, while mode E_2 has a maximum value at an angle of ∼45°. Our results suggest that the in-plane anisotropic properties of Se nanosheets could be easily identified by Raman spectroscopy. It could also be confirmed that the Se nanosheets are grown along the $\langle 1\bar{2}10\rangle$ direction, which matches well the STEM results.

Trigonal selenium possesses a highly anisotropic crystal structure. Under thermodynamic equilibrium conditions, it tends to grow into 1D structures along the [0001] direction. However, the products in our experiments exhibit a 2D structure with very small thickness, which is very different from the previous bulk Se. Time-dependent experiments were conducted to explore the growth mechanism of Se nanosheets. Figure 5a shows the typical morphology of products when the growth temperature just reaches 160 °C. Amorphous nanospheres with diameters ranging from 10 to 30 μm appeared on the Si substrate surface. With the temperature rising up to 210

DOI: 10.1021/acsnano.7b04786
ACS Nano 2017, 11, 10222−10229

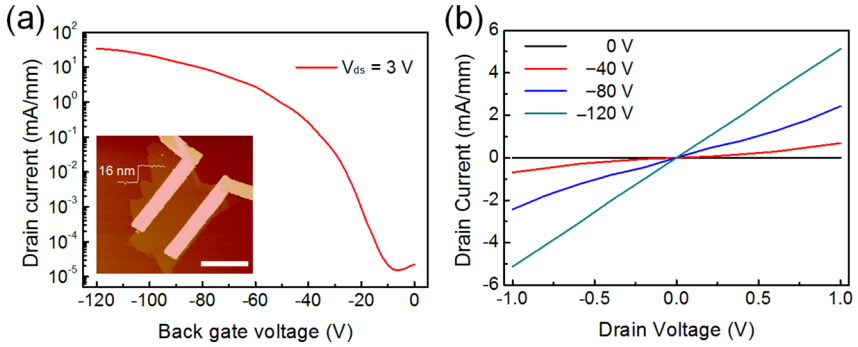

Figure 6. Se nanosheet FET device performance. (a) Transfer characteristic of a typical Se nanosheet field effect transistor with a thickness of 16 nm. Inset shows the AFM height profile of the device; scale bar is 5 μm. (b) Output characteristic of the same Se nanosheet transistor.

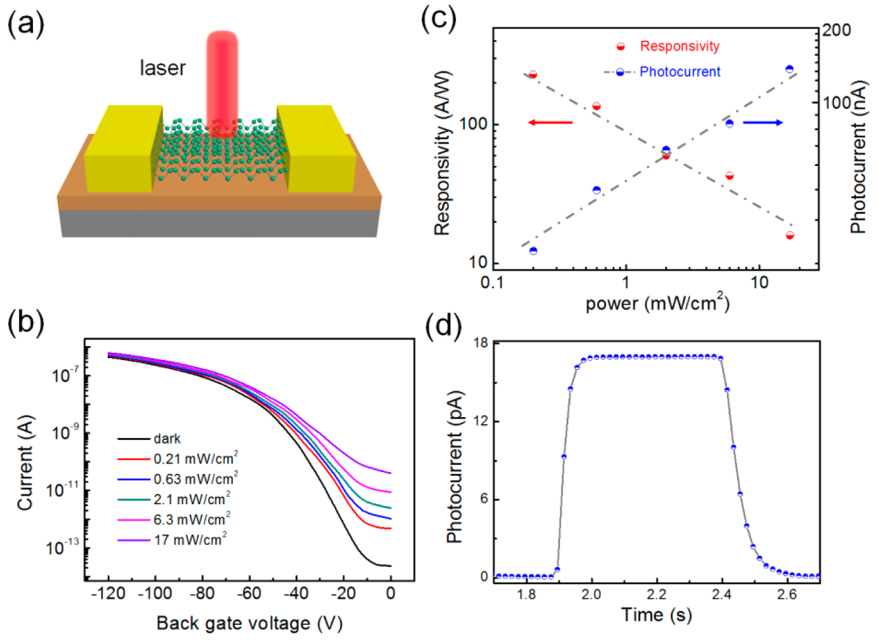

Figure 7. Photoelectrical properties of a Se nanosheet phototransistor. (a) Schematic diagram of a back-gated Se nanosheet phototransistor. (b) Transfer curves of a Se nanosheet phototransistor measured under various laser irradiation powers at V_{ds} = 3 V. (c) Photocurrent (I_{ph}) and responsivity (R_λ) as a function of laser illumination power measured at V_{ds} = 3 V and V_g = −80 V. The dotted line for I_{ph} is well matched with the data using the function $I_{ph} = P^\beta$, where P is the effective power of the illumination on the device and β is a constant. (d) Typical rise or decay characteristics of the photocurrent with the laser illumination switched on or off.

°C, amorphous nanospheres start to crystallize and form polycrystalline films, with numerous short nanorods protruding out of the surface (Figure 5b and Figure S4). Based on previous studies, heat treatment could accelerate the transformation of amorphous selenium to crystalline selenium,[27] and Imura *et al.* have successfully prepared polycrystalline films consisting of nanoparticles by *in situ* thermal treatment for photodetector applications.[28] The preferable growth of 1D Se nanorods is kinetically favored, since the binding energy of Se atoms along the *c*-axis is much higher than that along the ⟨1$\bar{2}$10⟩ directions.[16] Besides, these 1D nanorods possess high chemical activity especially at the vertexes and ridges, which could play the role of roots for the subsequent nanosheet growth.[29] Interestingly, as the reaction continues, the growth along the *c*-axis is partly hindered, and the nanorods tend to expand in parallel along the ⟨1$\bar{2}$10⟩ direction to form 2D thin nanosheets as shown in Figure 5c. Under the same magnitude of supersaturation, the growth of Se nanostructure is mainly driven by surface energy as well as effective activation sites count.[30] In the initial crystallization, 1D growth of the nanorod is dominant due to the distinct surface energy difference. However, after the nanorod has grown to a certain length, Se_2(g) molecules would seldom fall within the end cavity of a nanorod due to the large free path at such high temperatures.[30] It is more likely that they would impinge on the nanorod surface and diffuse from site to site until they encounter a defect or void of the crystal; thus the growth along the ⟨1$\bar{2}$10⟩ direction would be enhanced. Actually, at the lateral side of the Si substrate, where the downstream Se_2(g) molecules have greater odds of encountering a (0001) facet of the nanorod, the nanorod would continue to grow along the ⟨0001⟩ direction into the nanowire with lengths up to 200 μm (Figure S5). Figure 5d illustrates the products' morphology when the growth duration is up to 60 min; the nanorods have completely turned into long, saw-like ultrathin nanosheets.

The formation of Se nanosheets could be well explained by the vapor−solid (VS) growth mechanism,[30,31] and similar growth phenomena have been reported in the preparation of ZnSe nanobelts.[32] It is worth noting that some of the nanosheets exhibit a feather-like structure with mirror twins.

DOI: 10.1021/acsnano.7b04786
ACS Nano 2017, 11, 10222−10229

We believe that they were developed from sections of intersected nanorods, which are introduced at the initial crystalline stage (Figure S6). These crossed nanorods could act as growth roots and enable the identical lateral growth on both sides of the nanosheet, leading to the symmetrical structure.[33,34]

Se nanosheet FETs were fabricated using electron beam lithography (EBL), thermal evaporation, and a lift-off process. Ni/Au (30/100 nm) were selected as metal contacts, which could significantly reduce the contact resistance in p-type FET devices due to the relatively high work function.[35] Figure 6 shows the electrical characteristics of a typical Se nanosheet FET device with a channel thickness of 16 nm. It shows typical p-type transport behavior with a high current on/off ratio over 10^6. The presence of hydrogen and hydroxyl terminations on the nanosheets surface is considered to be the main reason for the p-type conduction of selenium FET, which has been demonstrated in Se nanowire and nanobelts.[17,36] The Se nanosheet FET presents a relatively low on-state current, with the maximum value around 20 mA/mm at V_{ds} = 3 V. Four-terminal field-effect devices are fabricated to evaluate the intrinsic hole mobility of Se nanosheets, as shown in Figure S7. The mobility could be extracted from the G *versus* V_{bg} curves in the $-100 < V_{bg} < -30$ V range using the expression $\mu = L_{in}/W \times (1/C_{bg}) \times dG/dV_{bg}$, and the value of hole mobility is expected to be 0.26 $cm^2 V^{-1} s^{-1}$ at 300 K. Compared with other p-type semiconductor materials such as tellurene and black phosphorus,[21,37−39] the Se nanosheet has a low hole mobility similar to those values reported in the literature on bulk selenium or selenium nanobelts.[40−42] Because of its low mobility and special band structure, it has the highest Seebeck coefficient (+1250 $\mu V K^{-1}$) among all elements and has the potential for thermoelectric applications. It is worth noting that the Se nanosheets and the transistors exhibit a good stability in ambient conditions (Figure S8). Even after 15 days' exposure to air, the surface morphology of the Se nanosheet almost does not change, and there is no significant degradation of device performance.

Selenium is known as an excellent material candidate for high-sensitivity optoelectronics. Herein, we also examine the optoelectronic performance of Se nanosheet phototransistors, and a schematic diagram is shown in Figure 7a. Figure 7b shows the I_{ds} curves as a function of V_g at various illumination power densities, exhibiting an obvious gate tunability of the photocurrent response of the Se nanosheet phototransistor. The device exhibits a pronounced photoresponse even at a very low illumination power down to 0.21 mW/cm^2, and the on-state photocurrent could reach up to 54 nA (Figure S9a). The enhancement of conduction under illumination confirms that the Se nanosheet could be used for low-noise, high-sensitivity optoelectronic applications.

Photoresponsivity (R_λ), defined as $R_\lambda = I_{ph}/PS$, is calculated to better evaluate the performance of the phototransistor, where I_{ph} is the generated photocurrent, P is the incident power, and S is the effective illuminated area. R_λ is estimated to be 263 A/W at an illumination power of 0.21 mW/cm^2 with V_{ds} = 3 V and V_{bg} = −80 V. This value is 4 orders of magnitude higher than the previously reported crystalline Se films grown by physical vapor deposition (17 mA/W with a bias of −10 V) and among the highest values reported for 2D materials.[43−47] The responsivity is linearly proportional to the power of the illumination as shown in Figure 7c, suggesting that the photocurrent is mainly determined by the photoexcited carriers.[48] Time-dependent photoresponse of laser ON and OFF is also measured at room temperature (Figure 7d). The response speed is characterized by a typical rise time of 0.10 s and decay time 0.12 s for V_{ds} = 3 V and V_{bg} = 0 V (taking a 10−90% photocurrent change for the rise times and 90−10% for the fall times). Figure S9b shows the photoresponse after four illumination cycles. The same level of photocurrent and noise with the laser switch demonstrates a stable and repeatable photoresponse of our device.

CONCLUSION

In summary, high-quality 2D Se nanosheets were successfully synthesized by the physical vapor deposition method. The as-synthesized Se nanosheet has a large lateral size up to 30 μm and a minimum thickness of 5 nm. The crystal structure of the 2D Se nanosheet and its growth mechanism have been studied. Back-gated FETs and four-terminal devices based on the Se nanosheet have been demonstrated, and the intrinsic carrier mobility is determined to be 0.26 $cm^2 V^{-1} s^{-1}$ at 300 K. The 2D Se nanosheet phototransistor exhibits an excellent photoresponsivity of 263 A/W, although the response time is slow. As a class of 2D materials formed by 1D van der Waals materials, Se nanosheets would have great potential in electronic and optoelectronic applications.

EXPERIMENTAL METHODS

Growth of Selenium Nanosheets. High-purity Se power (Sigma-Aldrich, 99.99%) was placed at the center of the heating zone in a multizone furnace, with a freshly cleaned Si(111) substrate located about 20−25 cm away from the powders. During the growth process, pure Ar gas was fed with a constant flow rate of 50 sccm. The tube pressure was maintained constant at 100 mbar. The whole reaction process was carried out under a temperature of 210 °C for the source and 100 °C for the substrate, and this temperature was maintained for 60 min. After the reaction was complete, a black-colored needlelike material coated on the Si substrate could be clearly indentified.

Raman and STEM Measurements. Raman measurement was performed using a HORIBA LabRAM HR800 Raman spectrometer. The system is equipped with a He−Ne excitation laser of 633 nm wavelength. The system was calibrated with the Raman peak of Si at 520 cm^{-1} before measurement. The incident laser was polarized along the [0001] direction of the selenium nanosheets and illuminated perpendicularly to the nanosheet surface. The polarized laser is parallel to spiral atom chains, and we denote this configuration as 0°. To avoid destroying the sample, the laser power is less than 1 mW. The HAADF-STEM was performed with a FEI Talos F200x equipped with a so-called probe corrector. This microscope was operated with an acceleration voltage of 200 kV.

Device Fabrication and Characterization. Selenium nanosheets were transferred onto 300 nm SiO_2/Si substrates using the Scotch tape method. Electron beam lithography was used to pattern electrodes, followed by electron beam evaporation of 30 nm Ni and 100 nm Au as metal contacts. The channel length L_{ch} was designed to be 4 μm, while the channel width W_{ch} = 10 μm. Four-terminal field-effect devices are also fabricated to evaluate the intrinsic hole mobility of Se nanosheets, the channel length L_{ch} between two voltage probes is 8.0 μm, and channel width W_{ch} is 4.0 μm. The devices were measured with a probe station connected to a semiconductor characterization system (4200SCS, Keithley) at room temperature. For photodetection, a 637 nm laser source (S1FC637, Perot Benchtop) calibrated by an UV-enhanced silicon photodiode was used to provide power-tunable irradiation.

DOI: 10.1021/acsnano.7b04786
ACS Nano 2017, 11, 10222−10229

ASSOCIATED CONTENT

Supporting Information

The Supporting Information is available free of charge on the ACS Publications website at DOI: 10.1021/acsnano.7b04786.

Schematic diagram of the transfer procedure, XPS, EDX, and EELS spectra of Se nanosheets, SEM image of Se microspheres and nanowires, air stability of Se nanosheets, four-terminal devices, and related measurement, and photoelectronic properties of Se nanosheets (PDF)

AUTHOR INFORMATION

Corresponding Author

*E-mail: yep@purdue.edu.

ORCID

Cheng-Yan Xu: 0000-0002-7835-6635
Haiyan Wang: 0000-0002-7397-1209
Peide D. Ye: 0000-0001-8466-9745

Author Contributions

#J. Qin and G. Qiu contributed equally to this work.

Author Contributions

P.D.Y. conceived the idea and supervised the experiments. J.K.Q. performed the growth experiments and analyzed the experimental data. J.K.Q. and G.Q. performed device fabrication and analyzed the experimental data. C.Y.X. and W.Z.W. analyzed the growth mechanism. H.Z. performed the SEM measurement. J.J. performed the STEM measurement. L.M.Y. and X.F.X. performed Raman measurement. A.R.C. and D.Z. performed and supervised the XPS analysis. H.Y.W. analyzed and supervised the STEM experiment. J.K.Q., G.Q., and P.D.Y. cowrote the manuscript.

Notes

The authors declare no competing financial interest.

ACKNOWLEDGMENTS

The authors would like to thank Chao Wang at Harbin Institute of Technology for the discussion on Raman measurements. J.K.Q. is supported by the Chinese Scholarship Council. The work is in part supported by the AFOSR/NSF EFRI 2DARE program, ARO, and SRC.

REFERENCES

(1) Kasap, S.; Frey, J. B.; Belev, G.; Tousignant, O.; Mani, H.; Laperriere, L.; Reznik, A.; Rowlands, J. A. Amorphous Selenium and Its Alloys from Early Xeroradiography to High Resolution X-ray Image Detectors and Ultrasensitive Imaging Tubes. *Phys. Status Solidi B* **2009**, *246*, 1794−1805.

(2) Suzuki, Y.; Yamaguchi, H.; Oonuki, K.; Okamura, Y.; Okano, K. Amorphous Selenium Photodetector Driven by Diamond Cold Cathode. *IEEE Electron Device Lett.* **2003**, *24*, 16−18.

(3) Oonuki, K.; Suzuki, Y.; Yamaguchi, H.; Okano, K.; Okamura, Y. Diode Structure Amorphous Selenium Photodetector with Nitrogen (N)-Doped Diamond Cold Cathode. *J. Vac. Sci. Technol., B: Microelectron. Process. Phenom.* **2003**, *21*, 1586−1588.

(4) Wang, K.; Chen, F.; Belev, G.; Kasap, S.; Karim, K. S. Lateral Metal-Semiconductor-Metal Photodetectors Based on Amorphous Selenium. *Appl. Phys. Lett.* **2009**, *95*, 013505.

(5) Abbaszadeh, S.; Allec, N.; Wang, K.; Karim, K. S. Low Dark-Current Lateral Amorphous-Selenium Metal−Semiconductor−Metal Photodetector. *IEEE Electron Device Lett.* **2011**, *32*, 1263−1265.

(6) Royer, D.; Dieulesaint, E. Elastic and Piezoelectric Constants of Trigonal Selenium and Tellurium Crystals. *J. Appl. Phys.* **1979**, *50*, 4042−4045.

(7) Lee, T. I.; Lee, S.; Lee, E.; Sohn, S.; Lee, Y.; Lee, S.; Moon, G.; Kim, D.; Kim, Y. S.; Myoung, J. M. High-Power Density Piezoelectric Energy Harvesting Using Radially Strained Ultrathin Trigonal Tellurium Nanowire Assembly. *Adv. Mater.* **2013**, *25*, 2920−2925.

(8) He, Z.; Yang, Y.; Liu, J.-W.; Yu, S.-H. Emerging Tellurium Nanostructures: Controllable Synthesis and Their Applications. *Chem. Soc. Rev.* **2017**, *46*, 2732−2753.

(9) Abad, B.; Rull-Bravo, M.; Hodson, S. L.; Xu, X.; Martin-Gonzalez, M. Thermoelectric Properties of Electrodeposited Tellurium Films and The Sodium Lignosulfonate Effect. *Electrochim. Acta* **2015**, *169*, 37−45.

(10) Sridharan, K.; Ollakkan, M. S.; Philip, R.; Park, T. J. Non-Hydrothermal Synthesis and Optical Limiting Properties of One-Dimensional Se/C, Te/C and Se−Te/C Core−Shell Nanostructures. *Carbon* **2013**, *63*, 263−273.

(11) Wang, R.; Su, X.; Bulla, D.; Wang, T.; Gai, X.; Yang, Z.; Madden, S.; Luther-Davies, B. In Identifying the Best Chalcogenide Glass Compositions for The Application in Mid-Infrared Waveguides. *Proc. SPIE* **2014**, 944406.

(12) Qian, J.; Jiang, K. J.; Huang, J. H.; Liu, Q. S.; Yang, L. M.; Song, Y. A Selenium-Based Cathode for a High-Voltage Tandem Photoelectrochemical Solar Cell. *Angew. Chem., Int. Ed.* **2012**, *51*, 10351−10354.

(13) Nguyen, D.-C.; Tanaka, S.; Nishino, H.; Manabe, K.; Ito, S. 3-D Solar Cells by Electrochemical-Deposited Se Layer as Extremely-Thin Absorber and Hole Conducting Layer on Nanocrystalline TiO_2 Electrode. *Nanoscale Res. Lett.* **2013**, *8*, 8.

(14) Zheng, L.; Hu, K.; Teng, F.; Fang, X. Novel UV−Visible Photodetector in Photovoltaic Mode with Fast Response and Ultrahigh Photosensitivity Employing Se/TiO_2 Nanotubes Heterojunction. *Small* **2017**, *13*, 1602448.

(15) Mondal, K.; Roy, P.; Srivastava, S. K. Facile Biomolecule-Assisted Hydrothermal Synthesis of Trigonal Selenium Microrods. *Cryst. Growth Des.* **2008**, *8*, 1580−1584.

(16) Ren, L.; Zhang, H.; Tan, P.; Chen, Y.; Zhang, Z.; Chang, Y.; Xu, J.; Yang, F.; Yu, D. Hexagonal Selenium Nanowires Synthesized *via* Vapor-phase Growth. *J. Phys. Chem. B* **2004**, *108*, 4627−4630.

(17) Luo, L.-B.; Yang, X.-B.; Liang, F.-X.; Jie, J.-S.; Li, Q.; Zhu, Z.-F.; Wu, C.-Y.; Yu, Y.-Q.; Wang, L. Transparent and Flexible Selenium Nanobelt-Based Visible Light Photodetector. *CrystEngComm* **2012**, *14*, 1942−1947.

(18) Reza, S.; Bosman, G.; Islam, M. S.; Kamins, T. I.; Sharma, S.; Williams, R. S. Noise in Silicon Nanowires. *IEEE Trans. Nanotechnol.* **2006**, *5*, 523−529.

(19) Bid, A.; Bora, A.; Raychaudhuri, A. 1/f Noise in Nanowires. *Nanotechnology* **2006**, *17*, 152.

(20) Wang, Y.; Qiu, G.; Wang, Q.; Liu, Y.; Du, Y.; Wang, R.; Goddard, W. A., III; Kim, M. J.; Ye, P. D.; Wu, W. Large-Area Solution-Grown 2D Tellurene for Air-Stable, High-Performance Field-Effect Transistors. *arXiv preprint arXiv.* **2017**, *1704*, 06202.

(21) Du, Y.; Qiu, G.; Wang, Y.; Si, M.; Xu, X.; Wu, W.; Ye, P. D. 1D van der Waals Material Tellurium: Raman Spectroscopy under Strain and Magneto-transport. *Nano Lett.* **2017**, *1704*, 07020.

(22) Wang, Q.; Safdar, M.; Xu, K.; Mirza, M.; Wang, Z.; He, J. Van der Waals Epitaxy and Photoresponse of Hexagonal Tellurium Nanoplates on Flexible Mica Sheets. *ACS Nano* **2014**, *8*, 7497−7505.

(23) Jiang, Z.-Y.; Xie, Z.-X.; Xie, S.-Y.; Zhang, X.-H.; Huang, R.-B.; Zheng, L.-S. High Purity Trigonal Selenium Nanorods Growth *via* Laser Ablation under Controlled Temperature. *Chem. Phys. Lett.* **2003**, *368*, 425−429.

(24) Shenasa, M.; Sainkar, S.; Lichtman, D. XPS Study of Some Selected Selenium Compounds. *J. Electron Spectrosc. Relat. Phenom.* **1986**, *40*, 329−337.

(25) Martin, R. M.; Lucovsky, G.; Helliwell, K. Intermolecular Bonding and Lattice Dynamics of Se and Te. *Phys. Rev. B* **1976**, *13*, 1383.

(26) Lucovsky, G.; Mooradian, A.; Taylor, W.; Wright, G.; Keezer, R. Identification of the Fundamental Vibrational Modes of Trigonal, α-

DOI: 10.1021/acsnano.7b04786
ACS Nano 2017, 11, 10222−10229

Monoclinic and Amorphous Selenium. *Solid State Commun.* **1967**, *5*, 113−117.
(27) Serra, A.; Rossi, M.; Buccolieri, A.; Manno, D.; Rossi, M.; Mariani, C.; Terranova, M. L. Solid-to-Solid Phase Transformations of Nanostructured Selenium-Tin Thin Films Induced by Thermal Annealing in Oxygen Atmosphere. *AIP Conf. Proc.* **2013**, 31−39.
(28) Imura, S.; Kikuchi, K.; Miyakawa, K.; Ohtake, H.; Kubota, M.; Nakada, T.; Okino, T.; Hirose, Y.; Kato, Y.; Teranishi, N. High Sensitivity Image Sensor Overlaid with Thin-Film Crystalline-Selenium-Based Heterojunction Photodiode. *IEEE Trans. Electron Devices* **2016**, *63*, 86−91.
(29) Wang, Q.; Li, G.-D.; Liu, Y.-L.; Xu, S.; Wang, K.-J.; Chen, J.-S. Fabrication and Growth Mechanism of Selenium and Tellurium Nanobelts through a Vacuum Vapor Deposition Route. *J. Phys. Chem. C* **2007**, *111*, 12926−12932.
(30) Hawley, C. J.; Beatty, B. R.; Chen, G.; Spanier, J. E. Shape-Controlled Vapor-Transport Growth of Tellurium Nanowires. *Cryst. Growth Des.* **2012**, *12*, 2789−2793.
(31) Pan, Z. W.; Dai, Z. R.; Wang, Z. L. Nanobelts of Semiconducting Oxides. *Science* **2001**, *291*, 1947−1949.
(32) Hu, Z.; Duan, X.; Gao, M.; Chen, Q.; Peng, L.-M. ZnSe Nanobelts and Nanowires Synthesized by a Closed Space Vapor Transport Technique. *J. Phys. Chem. C* **2007**, *111*, 2987−2991.
(33) Gamalski, A. D.; Voorhees, P. W.; Ducati, C.; Sharma, R.; Hofmann, S. Twin Plane Re-entrant Mechanism for Catalytic Nanowire Growth. *Nano Lett.* **2014**, *14*, 1288−1292.
(34) Soo, M. T.; Zheng, K.; Gao, Q.; Tan, H. H.; Jagadish, C.; Zou, J. Mirror-Twin Induced Bicrystalline InAs Nanoleaves. *Nano Res.* **2016**, *9*, 766−773.
(35) Sheu, J.; Su, Y.-K.; Chi, G.-C.; Koh, P.; Jou, M.; Chang, C.; Liu, C.; Hung, W. High-Transparency Ni/Au Ohmic Contact to P-type GaN. *Appl. Phys. Lett.* **1999**, *74*, 2340−2342.
(36) Belev, G.; Tonchev, D.; Fogal, B.; Allen, C.; Kasap, S. Effects of Oxygen and Chlorine on Charge Transport in Vacuum Deposited Pure a-Se Films. *J. Phys. Chem. Solids* **2007**, *68*, 972−977.
(37) Iqbal, M. W.; Iqbal, M. Z.; Khan, M. F.; Shehzad, M. A.; Seo, Y.; Park, J. H.; Hwang, C.; Eom, J. High-Mobility and Air-Stable Single-Layer WS_2 Field-Effect Transistors Sandwiched between Chemical Vapor Deposition-Grown Hexagonal BN Films. *Sci. Rep.* **2015**, *5*, 10699.
(38) Radisavljevic, B.; Radenovic, A.; Brivio, J.; Giacometti, i. V.; Kis, A. Single-Layer MoS_2 Transistors. *Nat. Nanotechnol.* **2011**, *6*, 147−150.
(39) Liu, H.; Du, Y.; Deng, Y.; Ye, P.D. Semiconducting Black Phosphorus: Synthesis, Transport Properties and Electronic Applications. *Chem. Soc. Rev.* **2015**, *44*, 2732−2743.
(40) Sharma, A. K.; Singh, B. Electrical Conductivity Measurements of Evaporated Selenium Films in Vacuum. *Proc. Indian Natn. Sci. Acad.* **1980**, 362−368.
(41) Spear, W. The Hole Mobility in Selenium. *Proc. Phys. Soc., London* **1960**, *76*, 826.
(42) Plessner, K. Conductivity, Hall Effect and Thermo-electric Power of Selenium Single Crystals. *Proc. Phys. Soc., London, Sect. B* **1951**, *64*, 671.
(43) Zhai, T.; Fang, X.; Liao, M.; Xu, X.; Li, L.; Liu, B.; Koide, Y.; Ma, Y.; Yao, J.; Bando, Y. Fabrication of High-Quality In_2Se_3 Nanowire Arrays toward High-Performance Visible-Light Photodetectors. *ACS Nano* **2010**, *4*, 1596−1602.
(44) Tao, X.; Gu, Y. Crystalline−Crystalline Phase Transformation in Two-Dimensional In_2Se_3 Thin Layers. *Nano Lett.* **2013**, *13*, 3501−3505.
(45) Xia, J.; Zhu, D.; Wang, L.; Huang, B.; Huang, X.; Meng, X. M. Large-Scale Growth of Two-Dimensional SnS_2 Crystals Driven by Screw Dislocations and Application to Photodetectors. *Adv. Funct. Mater.* **2015**, *25*, 4255−4261.
(46) Zhou, X.; Zhang, Q.; Gan, L.; Li, H.; Zhai, T. Large-Size Growth of Ultrathin SnS_2 Nanosheets and High Performance for Phototransistors. *Adv. Funct. Mater.* **2016**, *26*, 4405−4413.
(47) Yin, Z.; Li, H.; Li, H.; Jiang, L.; Shi, Y.; Sun, Y.; Lu, G.; Zhang, Q.; Chen, X.; Zhang, H. Single-Layer MoS_2 Phototransistors. *ACS Nano* **2011**, *6*, 74−80.
(48) Li, X.; Cui, F.; Feng, Q.; Wang, G.; Xu, X.; Wu, J.; Mao, N.; Liang, X.; Zhang, Z.; Zhang, J. Controlled Growth of Large-Area Anisotropic ReS_2 Atomic Layer and Its Photodetector Application. *Nanoscale* **2016**, *8*, 18956−18962.

DOI: 10.1021/acsnano.7b04786
ACS Nano 2017, 11, 10222−10229